ADVANCED NANOMECHANICAL TESTING

Quantifying surface deformation around micrometer-scale indents by digital image correlation

Mengying Liu[1,a] , Ian McCue[1,2], Michael J. Demkowicz[1]

[1] Department of Materials Science and Engineering, Texas A&M University, College Station, TX 77843, USA
[2] Research and Exploratory Development Department, The Johns Hopkins University Applied Physics Laboratory (JHU/APL), Laurel, MD 20723, USA
[a] Address all correspondence to this author. e-mail: myliu@tamu.edu

Indentation tests provide a facile route to gathering strength and stiffness information from small-scale samples, but typically have not been used to systematically assess distributions of surface plastic strain. The objective of the present work is to quantify in-plane plastic strain around micrometer-scale indents via digital image correlation (DIC). We demonstrate the method by comparing pre- and post-indentation surface images, acquired with a scanning electron microscope (SEM). Applying this method to metal composites synthesized by liquid- and solid-metal dealloying, we find that the maximum surface strains around indents do not change with the indentation depth, that strain concentrates preferentially in regions with largest composite constituent dimensions, and that the constituents are not co-deforming. We conclude that the method we have demonstrated is suitable for characterizing the relative propensity of materials to undergo uniform or localized plastic flow.

Introduction

Indentation load–displacement curves provide a facile route to characterizing the strength and stiffness of small-scale material samples [1, 2]. The distribution of surface plastic strain around indents is also of fundamental scientific interest and may give additional insight into material properties [3–8]. For example, surface strain distributions around micrometer-scale indents may shed light on a material's propensity for uniform vs. localized flow [9], as well as the influence of individual components in a multiphase material on the overall mechanical response. To that end, changes in surface topography around micrometer-scale indents are routinely characterized by atomic force microscopy (AFM) [10–12]. However, to date, there has not been a facile method for characterizing the in-plane strain distribution on the material surface around an indent. We demonstrate a method for quantifying surface plastic strain around micrometer-scale indents by comparing pre- and post-indentation images, acquired by scanning electron microscopy (SEM), using digital image correlation (DIC).

Experimental approaches to determining surface strains involve comparing images before and after indentation. One such technique is Electron Backscatter Diffraction (EBSD) cross-correlation [13, 14], which compares Kikuchi patterns collected at individual locations to determine deformation. The magnitude and directions of the pattern shift vary systematically with position across the EBSD pattern, allowing variations in elastic strain and small lattice rotations to be determined [15]. EBSD cross-correlation only provides relative variation in elastic strain and cannot be used to assess plastic strain. It cannot be applied to amorphous solids, where Kikuchi patterns cannot be collected. Moreover, it requires ultra-high-quality surface polishing, a high speed EBSD detector, and extensive data analysis.

Another approach to surface strain determination is DIC, which may be used to characterize surface plastic strains [16]. DIC analysis has been applied to optical images of millimeter-scale indents, yielding a maximum in-plane spatial resolution of 50 μm [16]. Higher resolution strain maps have been obtained by applying DIC to images acquired by SEM [17, 18]. For example, Stinville et al. have used SEM-DIC to identify slip bands in Ni-base superalloys during cycling loading [19, 20]. In that study, SEM-DIC provides spatial resolution of < 500 nm while maintaining the accuracy of calculated strain. It is therefore suitable to obtain strain field distributions within the small area surrounding micrometer-scale indents. Indeed, the spatial

resolution of the measurement we report here is at the submicron level, far beyond that reported in any previous DIC study of indentation [21, 22], including the few that imaged surfaces using a SEM [23].

We apply our method to WCuTi dealloyed nanocomposite samples. These materials consist of two phases, which show high contrast under the SEM [24]. Similar to Stinville et al. [19], we use the inherent microstructure morphology of in our samples as a pattern for subsequent DIC. This approach obviates the need to deposit an extrinsic pattern of nanoparticles and avoids any extraneous influence of such a pattern on mechanical response [25]. We analyzed the indentation-induced surface strain distribution as a function of indentation depth and indenter angle. For samples with comparable microstructure feature dimensions, the maximum magnitude of surface strain does not change with the indentation depth. In addition, strain concentrates preferentially in areas with larger microstructure feature dimensions. Finally, we find that the constituent phases in WCuTi composites do not perfectly co-deform.

Characterizing strain fields via SEM-DIC

Our method for characterizing plastic strain fields around indents comprises five steps: (1) Generation of fiducial markers for pre- and post-indentation image alignment; (2) Acquisition of an image of the test region prior to indentation; (3) Indentation within the test region; (4) Acquisition of an image of the test region after indentation; (5) Comparative analysis of the pre- and post-indentation images using DIC. In this study, we characterized WTi/CuTi nanocomposites processed by liquid metal dealloying (LMD) and solid metal dealloying (SMD). The synthesis of these samples, SEM imaging parameters, and indentation process are detailed in the "Methodology" section.

SEM imaging of the surfaces shows that both the LMD and the SMD materials consist of two interpenetrating metal phases: one W-rich (bright) and the other Cu-rich (dark) (Fig. 1). The interpenetrating phases form ligaments, whose characteristic dimensions and interconnectivity can be changed by altering the alloy compositions and processing conditions [26]. We determined the characteristic ligament dimensions of those two phases using the AQUAMI image analysis tool [27]. The characteristic ligament dimension of the W-rich phase is 250 ± 150 nm in the LMD sample, and ranging from 32.9 ± 11.7 nm to 84.8 ± 26.4 nm in SMD samples.

We applied a 7 N load on the LMD sample surface, and 30 mN, 50 mN, 70 mN, 100 mN, 250 mN, 500 mN, and 1 N at different locations on the SMD samples. Hardness and modulus values were inferred from load–displacement curves using the Oliver-Pharr method [1]. We carried out 2-D DIC analysis of pre- and post-indentation images using Ncorr [28], a freely available MATLAB-based graphical user interface code. Ncorr
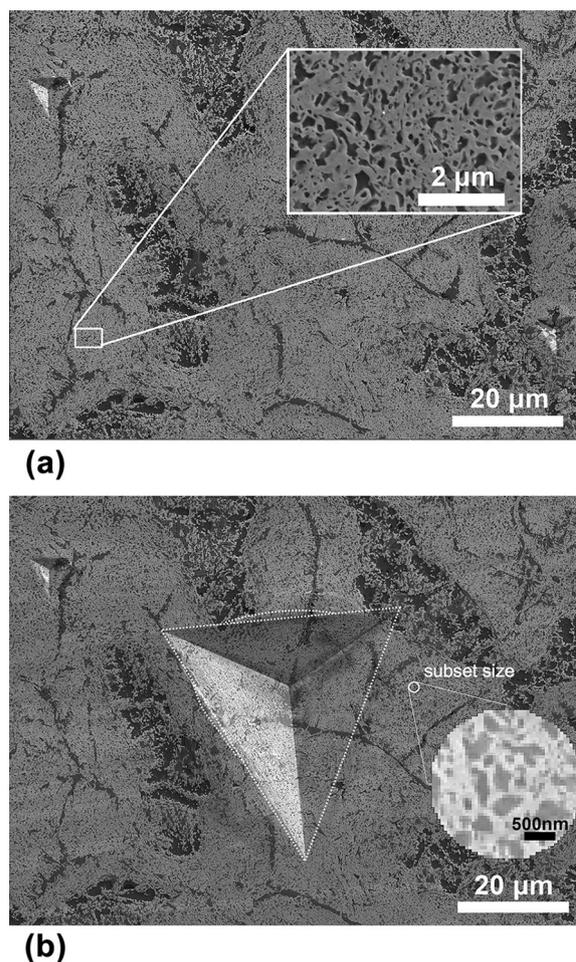

(a)

(b)

Figure 1: (a) Pre-indentation image of the LMD WTi/CuTi sample. The indents in the top-left and bottom-right corners are fiducial markers used for image alignment. The inset shows a magnified view of the bicontinuous sample microstructure. (b) Post-indentation image of the area shown in (a). Dashed lines show the nominal indent shape as well as regions where material piled up against the indenter. The small circle illustrates a subset of 25-pixel radius: the size used in our DIC analysis. The inset shows a magnified SEM image of the subset.

outputs displacement maps and the associated 2-D Eulerian strain tensors, from which we then calculate surface hydrostatic and deviatoric strains.

Resolution adjustment and noise reduction

An in-depth description of the Ncorr algorithm may be found in Ref. [28]. Instead of relying solely on grayscale matching and 4-point interpolation, Ncorr correlates image subsets to calculate displacement fields. This approach improves the precision of the correlation and reduces the computational overhead. Subsets are sets of pixels within circular areas of specified radius centered at an individual pixel in the region of interest (ROI), as illustrated in Fig. 1b. The deformation is assumed to be homogeneous inside each subset. Ncorr interpolates sub-pixel

Article

displacements using biquintic b-splines and uses a reliability-guided method to obtain displacement values for all subsets.

We use Reu's method [29] with 20% cut-off to determine the spatial resolution and noise of Ncorr under each subset radius and strain window. Spatial resolution is defined as the distance over which changes in strain are measurable above the noise floor, thus, it is related to precision. A large subset size smooths the results and returns poor spatial resolution while small subset size increases spatial resolution and magnifies noise. Figure 2a plots the spatial resolution and noise we determined for a range of subset diameters.

For optimal DIC accuracy, each subset should ideally contain at least 2–3 ligament features to correlate, and each ligament should contain 2–5 pixels [30]. Too few pixels within each surface feature leads to undersampling, yielding poor accuracy in the spatial derivative of the estimated displacement field. However, too many pixels within each ligament leads to oversampling, which means that—for a fixed number of pixels in an image subset—there are fewer features available for inferring the local displacement.

The indent size must be significantly larger than the characteristic length of the DIC pattern in order to acquire location-dependent variations of the strain field. Based on the aforementioned DIC image parameters and the spatial resolution to pixel size relationship in Fig. 2a, we conclude that the indent should be at least ten times larger than the subset dimensions. For any given material, larger indents with higher load will generate larger regions of plastic deformation. Only when the plastic region around the indent is larger than the spatial resolution can the surface strains around the indent be computed.

With the calculated relationship between spatial resolution and subset diameter (Fig. 2a), we take the suggested optimal DIC settings (2–3 ligaments per subset, 2–5 pixels per ligament), and then plot the spatial resolution vs. pixel size, with ligament size ranges from 40 to 80 nm. Assuming that inter-ligament spacing is equal to ligament size, the optimal number of pixels within a subset is twice the number of pixels within a ligament. As shown in Fig. 2b, finer DIC patterns are helpful for reaching a better spatial resolution. Although fewer pixels and ligaments provide better spatial resolution in theory, in practice one cannot ignore the poor correlation accuracy due to undersampling and high noise level that arise in this limit.

The strain resolution is limited by two types of noise inherent in our SEM imaging: signal noise and drift artifacts. High magnification and long dwell time reduce signal noise, but may lead to more pronounced drift artifacts, which take the form of horizontal or vertical stripes in the acquired image. Lower magnification with shorter dwell time may reduce drift artifacts, but increases signal noise [19, 31]. These two sources of noise give rise to a detection limit: a lower bound on the magnitude of strains that may be resolved.
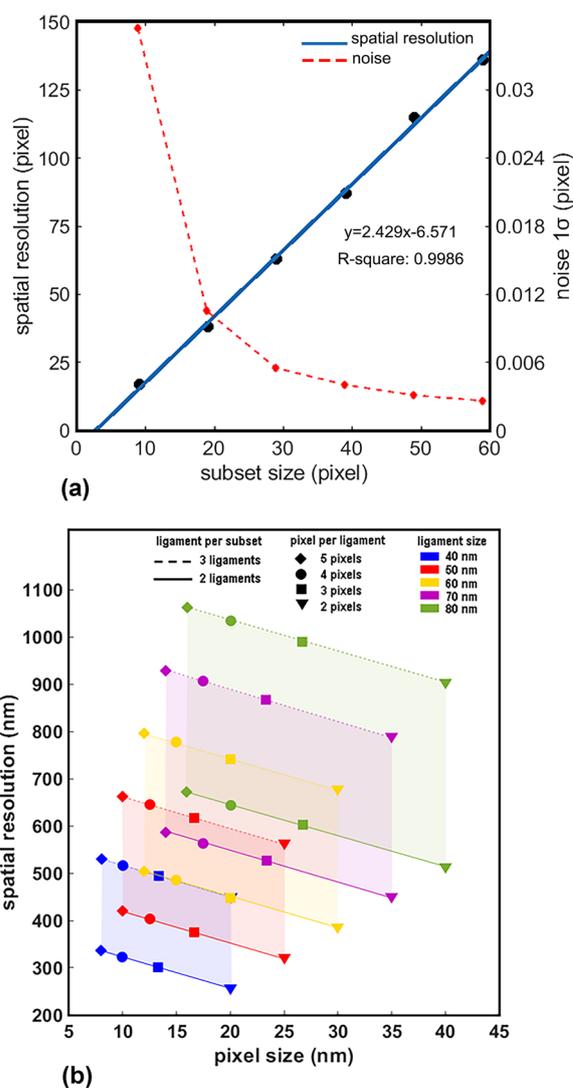

Figure 2: (a) Plot of spatial resolution and noise in pixels, as determined by Reu's method [29], for a range of subset diameters. Black dots are the tested spatial resolution results of 9, 19, 29, 39, 49, 59 pixels in subset diameter, and the blue solid line is the linear regression for the subset size and spatial resolution relationship. Red dots and the dashed line are the tested noise results of 9, 19, 29, 39, 49, 59 pixel in subset diameter. (b) Plot of spatial resolution in nm for a range of SEM pixel sizes, with the setting of different ligament size (40 nm in blue, 50 nm in red, 60 nm in yellow, 70 nm in purple, and 80 nm in green), ligament per subset (2 in solid line, 3 in dashed line), and pixel per ligament (2 in triangle, 3 in square, 4 in round, and 5 in diamond).

We characterized the detection limit by performing DIC on pairs of theoretically identical SEM images. Kammers et al. have also used this approach together with a rigid displacement between the pair of collected images to evaluate both spatial and drift distortion [31]. In our case, we take two SEM images of the same location with no indentation or any other modification applied. To mimic the actual experimental condition, after taking the first image, we take the sample out of the SEM chamber, reload it again, and then take the second image. By

www.mrs.org/jmr

June 2021

Issue 11

Volume 36

Journal of Materials Research

2279

doing so, we not only take signal noise and drift distortion into consideration, but also account for perturbations arising from removing and re-mounting the sample in the SEM, and SEM chamber conditions. We then use Ncorr to perform DIC on this pair of theoretically identical images. For completeness, the surface strain component maps for all parameter combinations we used are shown in the supplementary material (Fig. S1). Ideally, all the surface strain components, ε_{xx}, ε_{yy}, and $\varepsilon_{xy} = \varepsilon_{yx}$, ought to have null values. However, due to the aforementioned sources of noise, their values are in fact non-zero.

To identify a detection limit, we find the distribution of strain values from the theoretically identical pairs. For each strain component, we take the strain values of all pixels, and plot the distribution. Since these distributions generally span over both positive and negative strain values, we define an upper and lower detection limit for each. The lower value is set as the strain that bounds the lower 5% of the total distribution or zero, whichever is smaller. The upper value is the strain that bounds the lower 95% of the total distribution or zero, whichever is greater. For any strain map determined using the same image and DIC settings (magnification, dwell time, subset size, etc.) as the detection limit calculation, strain values with magnitudes greater than the applicable (upper or lower) detection limits are considered reliable. Any strains with magnitudes that fall below the detection limit are not considered reliable and are not plotted in the strain maps reported in the subsequent sections. For quantities that are functions of individual strain components, such as hydrostatic strain or the norm of the deviatoric strain, we compute values using only those strain components that are above their detection limit. Consequently, in hydrostatic and deviatoric strain maps, locations with no color correspond to strains that fall below the detection limit. For each DIC analysis presented below, we sweep across different DIC parameters and select the ones that offer an acceptable balance between spatial resolution and detection limit.

With the foregoing considerations in mind, for LMD samples, we use a relatively large indent area with edge ~ 60 μm in length, i.e. much larger than the ~ 250 nm dimensions of the microstructure pattern. We pick a subset radius of 25 pixels, with each pixel spanning ~ 50 nm (Fig. 1b inset). There are approximately 4–5 dark ligament features across the diameter of the subset. This choice yields a spatial resolution up to 115 pixels (4 μm, in our case). We did not determine a detection limit for the LMD samples. For SMD samples, whose ligament sizes range from 32.9 ± 11.7 nm to 84.8 ± 26.4 nm, we used indents with edge lengths no shorter than 4 μm, which is much larger than the average ligament size (50 nm). We choose the resolution of the SEM image (from 7 to 23 nm) based on the ligament size (specific parameters for each sample are listed in Table 1). We pick the optimal condition of 14–30 pixels subset radius, and 1 pixel step size (0 skipped pixels) to obtain displacement maps. These settings yield a spatial resolution of 55–130 pixels, according to Fig. 2a. For both LMD and SMD samples, the surface strains were calculated from displacements [32] using a 5×5 pixels strain window.

Edge effects in post-indentation SEM images

In addition to Berkovich tips, we also attempted to apply our DIC analysis to indents made with cube corner, 45°, and 55° tips. However, we were not able to characterize the surface strains in these indents due to the abrupt changes in brightness around the edges of these indents (see Supplementary Fig. S2a). The indent edges are much brighter than surrounding areas with the over-bright zone having dimensions comparable to the size of the plastically deformed region around the indents. The difference in brightness and contrast in pre- and post-indentation images proved too large to allow for reliable inference of strain fields using DIC.

TABLE 1: Ligament size, indentation data, and DIC parameters for locations A through L.

Location	Ligament dimension (nm)	Maximum indentation load (mN)	Modulus (GPa)	Hardness (GPa)	Pixel size (nm)	Subset radius (pixels)	Subset diameter(nm)
A	Upper: 75.777 ± 21.447 Lower: 61.330 ± 19.182	500	156.21	6.21	23.438	25	1171.9
B	Upper: 67.927 ± 21.104 Lower: 55.771 ± 16.584	250	164.98	6.36	15.625	25	781.25
C	56.673 ± 17.018	73	171.48	6.88	13.021	20	521.24
D	59.317 ± 16.794	50	178.62	7.50	13.021	20	521.24
E	58.571 ± 16.567	30	181.93	7.77	13.021	20	521.24
F	Upper: 84.805 ± 26.441 Lower: 68.251 ± 21.085	250	147.41	7.26	19.531	20	781.24
G	Upper: 37.787 ± 14.398 Lower: 78.909 ± 25.875	500	131.40	8.95	19.531	20	781.24
H	45.222 ± 17.164	100	128.32	8.59	7.3242	30	439.45
I	39.322 ± 14.151	500	80.30	7.66	16.276	14	472.00

The aforementioned over brightness is an artifact of SEM imaging. In SEM, the detector collects more secondary electrons from sharp edges than from flat surfaces, which makes indent edges appear brighter than the surrounding area [33]. Furthermore, as the standard secondary electron detector is not perpendicular to the sample stage, there is a brightness bias due to surface inclination with respect to the detector. More abrupt surface inclination changes give rise to higher brightness and bias. Therefore, edge effects are more pronounced when imaging small indents (created using loads lower than ~12 mN) with high-angle indenters (i.e., cube corner, 45°, and 55°).

For Berkovich indents, these artifacts influence the brightness slightly on the indent edge, but more so on the flat wall of the indented area. As we have excluded this area from our ROI, the brightness on the wall does not influence the image correlation for the rest of the image. To confirm that our calculated strain fields are not influenced by edge effects, we rotate the stage by 180° (altering the inclination of the indenter surfaces with respect to the detector) and re-compute our DIC strain maps. Although the pyramid walls show bias brightness, the strain fields are unaltered.

In-plane DIC demonstrated on LMD sample

Figure 1 shows the surface of the WTi/CuTi LMD sample before and after indentation. The small indents in the top-left and bottom-right corners of Fig. 1a are fiducial markers used for image alignment in DIC. The indent in the middle of the region shown in Fig. 1b is the main, 7 N indent, with an approximate depth of 5 μm and area of 1200 μm². This indentation test reports a

hardness of 5.9 GPa and an elastic modulus of 153 GPa (see Supplementary Figure Fig. S3), consistent with previously reported values for these composites [24]. Due to the significant elastic unloading of the indented surface upon removal of the indenter, the maximum depth of indentation on the load–displacement curve is greater than the indent depth measured by AFM.

As illustrated by the dashed lines in Fig. 1b, the edges of the indent are not perfectly straight. Instead, they are slightly curved due to material pile-up adjacent to the indenter faces during testing. Visual inspection of the large indent in Fig. 1b reveals no other obvious evidence of plastic strain concentrations. However, quantitative strain field analysis via DIC gives greater insight into the strain distribution around the indent. For this analysis, we select a ROI that excludes a triangular region containing the indent as well as the pile-up regions along the indenter edges, indicated in Fig. 3. The subset radius is 25 pixels and the strain window is 5 × 5 pixels, with 0 pixels skipped during the calculation.

Individual surface strain components obtained from DIC are shown in Fig. 3a–c, where yellow corresponds to positive (tensile) strain and blue corresponds to negative (compressive) strain. The strain field in Fig. 3a shows a localized region of positive strain near the top edge of the indent with a value of 0.039, and a localized region of negative strain near the left edge with a value of −0.082. The strain field in Fig. 3b shows concentrations of both positive and negative (−0.031) strain near the top edge, positive strain (0.046) near the left edge, and negative strain near the right edge. The strain field in Fig. 3c shows a localized region of negative strain at the top edge with a value of −0.074, and a localized region of positive strain near the left
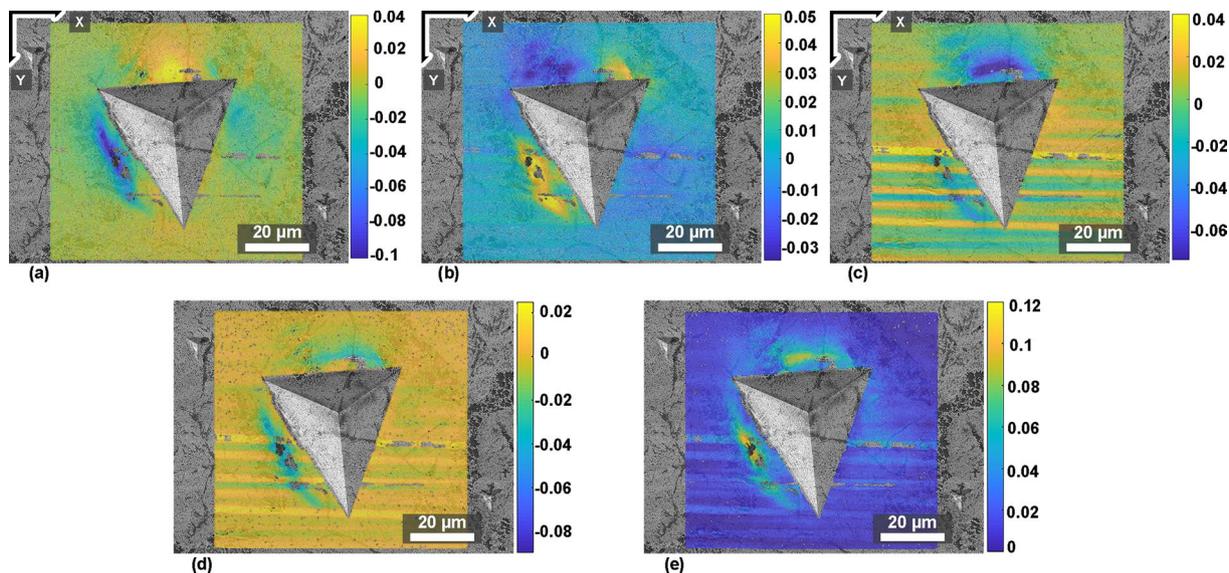

Figure 3: Surface strain field around the 7 N indent shown in Fig. 1b: (a) ε_{xx}, (b) $\varepsilon_{xy} = \varepsilon_{yx}$, (c) ε_{yy}, (d) the hydrostatic strain, and (e) the norm of the deviatoric strain (calculated from the surface strain components from a–c). Bands of elevated strain are apparent ~10 μm above the top edge and ~10 μm beside the left edge of the indented area.

edge. Additionally, there are horizontal stripes across the ROI in Fig. 3c. These features are artifacts associated with beam drift during SEM image acquisition.

The strain maps in Fig. 3a–c confirm the ability of DIC to characterize deformation in the vicinity of a small-scale indent. To gain greater insight into the plastic flow patterns thereby revealed, we compute two invariants of the strain field: the hydrostatic strain, $\varepsilon_{hyd} = \frac{1}{2}\left(\varepsilon_{xx} + \varepsilon_{yy}\right)$, and the 2-norm of deviatoric strain, $\varepsilon_{dev} = \left|\boldsymbol{\varepsilon} - \mathbf{I}\varepsilon_{hyd}\right|$. Note that our DIC analysis is only able to determine the surface strain components, ε_{xx}, ε_{yy}, and $\varepsilon_{xy} = \varepsilon_{yx}$. Thus, our calculation of ε_{hyd} and ε_{dev} ignores all remaining strain components ($\varepsilon_{zz}\varepsilon_{xz} = \varepsilon_{zx}$ and $\varepsilon_{zy} = \varepsilon_{yz}$), representing the strain tensor as a 2×2 matrix. Consequently, ε_{hyd} and ε_{dev} should not be understood as characterizing the full, 3-D strain field at the surface, but rather as convenient measures of areal dilatation and shear, respectively.

Figure 3d and e show surface maps of ε_{hyd} and ε_{dev}, respectively. Both quantities are concentrated into rings around the top and left edges of the indent, indicating regions of locally elevated plastic strain. The shapes of these regions are consistent with extended surface slip bands due to sub-surface zones of concentrated plastic strain away from the indenter faces. To validate this interpretation, we performed an AFM scan to obtain the surface profile shown in Fig. 4. This measurement confirms that material ~ 10 μm away from the top and left edges of the indent forms an extended slip step, with a height of approximately 1 μm. In addition, AFM reveals a slightly elevated region on the bottom right edge of the indent. This region also exhibits a moderate deviatoric strain, as evidenced by the lighter blue color in Fig. 3b. As the ROI boundary of the strain map is offset from the indentation edge, part of this elevated region might not be included in the ROI, and thus does not appear as pronounced in the strain map as in the AFM scan.

In SEM, a change of surface inclination leads to a change in the yield of secondary electrons, and as a result, a change of contrast. The inclination of areas with increased surface elevation (Fig. 4) is no more than 10 degrees. According to Seiler [33], + 10° inclination from a surface perpendicular to the beam leads to 0.7% contrast intensity difference. We assessed the effect of this difference on inferred strain fields by running DIC on a pair of artificially generated images with up to 1% contrast difference. The contrast-induced differences in strains thereby obtained are 10^{-4}, well below the detection limit of our measurements and lower than other sources of uncertainty.

In-plane DIC analysis on SMD samples

We applied our DIC method to investigate surface plastic strains around indents performed on our SMD specimens. For these samples, the indentation tests were conducted at loads no greater
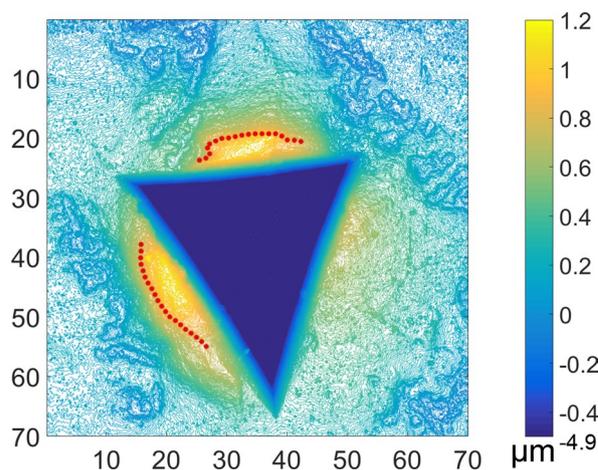

Figure 4: Surface profile of the area around the indent acquired using AFM, with unit all in μm. Regions where the surface elevation rapidly increases—indicated with dotted lines—are coincident with the bands of elevated strain shown in Fig. 3(d), (e).

than 1 N, resulting in negligible topographical changes. We obtained the 3-D surface profiles of indents A-D and F-I using laser confocal microscopy (see "Methodology" section), and the largest pile-up we observed is no more than 200 nm, at the edge of indent A, as shown in Supplementary FIG. S4. Outside the near-edge region, the out-of-plane displacement was never more than 60 nm, and the inclination angle of the surface based on the data in Fig. S4b is no more than 1°. This inclination is less than the 10° inclination we measured in LMD samples. It therefore yields uncertainties in surface strains below 10^{-4}, as discussed in the preceding section ("In-plane DIC demonstrated on LMD sample" section). Therefore, similar to the LMD sample, we exclude regions of significant out-of-plane displacement (the near-edge areas) from the ROI of our DIC analysis, limiting the analysis instead to areas where the displacement can reasonably be approximated as being in-plane only. The error in the inferred surface strains arising from the neglect of out-of-plane displacements in the region analyzed by DIC is acceptably low for the present application.

We investigated the influence of indent depth and location on strain distributions. Moreover, since our SMD samples exhibit a range of characteristic microstructural feature dimensions, we also assessed potential correlations between these dimensions and the material's indentation response. Table 1 lists indentation, microstructure, and imaging data for each indent. We do not observe any systematic variation in hardness or modulus with ligament dimensions. The number of indents carried out in this study maybe insufficient to reveal possible relationships between hardness (or modulus) and ligament size.

To assess the effect of indentation depth on surface strains, indents were performed using Berkovich tips at five locations
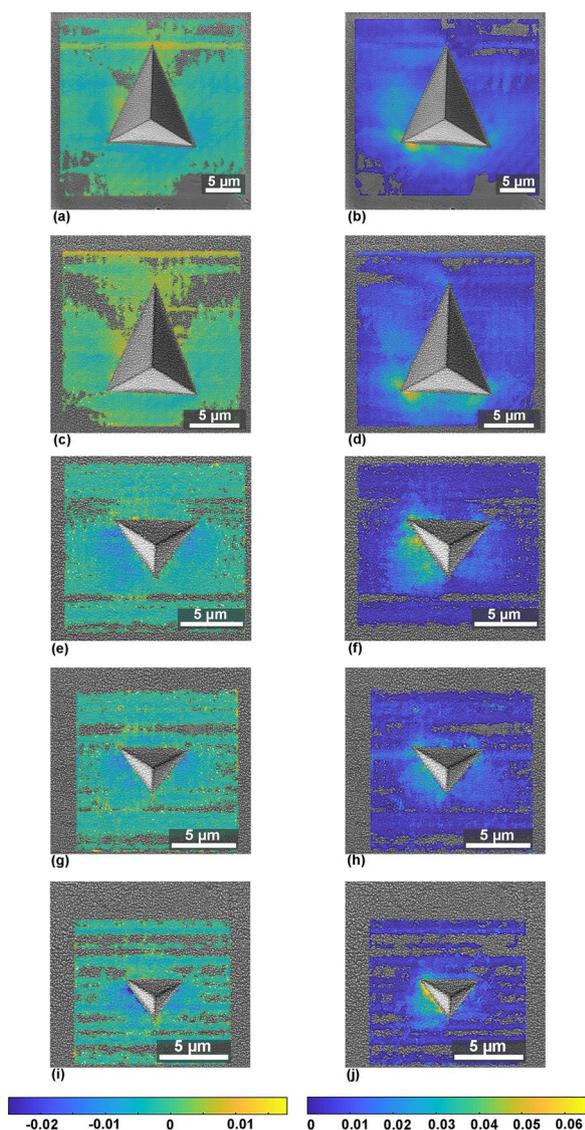
Figure 5: Surface hydrostatic strain fields for (a) A, (c) B, (e) C, (g) D, and (i) E. The norm of deviatoric strain of (b) A, (d) B, (f) C, (h) D, and (j) E. Each column of figures is associated with a single color bar, shown at the bottom. Locations with no color correspond to strains that fall below the detection limit.

(A, B, C, D, and E) with similar ligament dimensions (~ 59 nm). Peak loads from 30 to 500 mN were investigated. As shown in Table 1, as the indentation load decreases from 500 to 30 mN, the measured hardness increases from 6.21 to 7.26 GPa while the modulus increases from 156.21 to 181.93 GPa. This trend is attributed to the micro-indentation size effect [34]. We took pre- and post- indentation SEM images and then used DIC to obtain the strain distribution around these indents. Figure 5 plots the surface hydrostatic and deviatoric strain maps superimposed on SEM images of the indented regions. Locations with no color are ones where the inferred strain falls below the detection limit and is therefore not plotted.

Examining the data shown in Fig. 5, we find that different indent depths return similar strain values: max. hydrostatic strain around − 0.015, max. deviatoric strain ~ 0.06, average deviatoric strain in the concentrated plastic deformation area (colored green and light blue in Fig. 5) of ~ 0.045. Such consistency in the surface strains is expected because the strain fields induced by indentation are self-similar with respect to indent depth. However, the locations that exhibit peak strains vary from sample to sample. In indents A and B, the peak strain is located at the bottom edges of the indents. In C, D, and E, the peak strain is located at left edges of the indents.

For all indents, the ligament sizes are similar, and we have ruled out drift noise and edge effects (see "Resolution adjustment and noise reduction" and "Edge effects in post-indentation SEM images" sections above). Thus, we believe that the observed differences in strain distributions arise form unlike tip alignments with respect to the sample surface. Tip alignment may be expected to change between tests due to mounting differences for either the sample or the indenter tip. Indeed, indents A and B were performed one after another in a single set of tests while indents C, D, and E were also performed as a group, but in a different set of indent tests. We conclude that surface strains are a sensitive probe for assessing tip alignment during small-scale indents.

To assess the effect of ligament dimensions on surface strains, indents were performed using Berkovich tips at four locations (F, G, H, and I) with different characteristic microstructural dimensions. Two of these locations (F and G) exhibit a gradient in microstructural dimensions across the image area. The extrema in these dimensions are listed in Table 1. The strain maps we obtained, shown in Fig. 6, suggest that strain concentrates preferentially in regions with largest ligament dimensions. For example, in indent F, where the sample contains a gradient of ligament dimensions ranging from 85 to 68 nm, strains are concentrated mainly around the part of the indent closer to the region with larger ligament size. In that area, we measure a maximum deviatoric strain of ~ 0.08. Similarly, for G, the strain is also concentrated near the area with larger ligament sizes, with a maximum value of ~ 0.07. Moreover, examining all indents A through I, we see that as ligament sizes decrease from 85 to 39 nm, maximum deviatoric strains drop from 0.08 to 0.05, as shown in Fig. 7. Thus, our DIC analysis was effective at demonstrating that, in the SMD samples investigated here, smaller microstructure feature dimensions give rise to lower peak strain values and smoother variations of plastic flow.

Isolated microstructural heterogeneities also have a pronounced effect on surface strain fields around indents. An extreme example may be seen in Fig. 8, where one ligament is much larger than the surrounding ones, forming a Cu-rich vein. Several slip bands localize near this vein, as evidenced
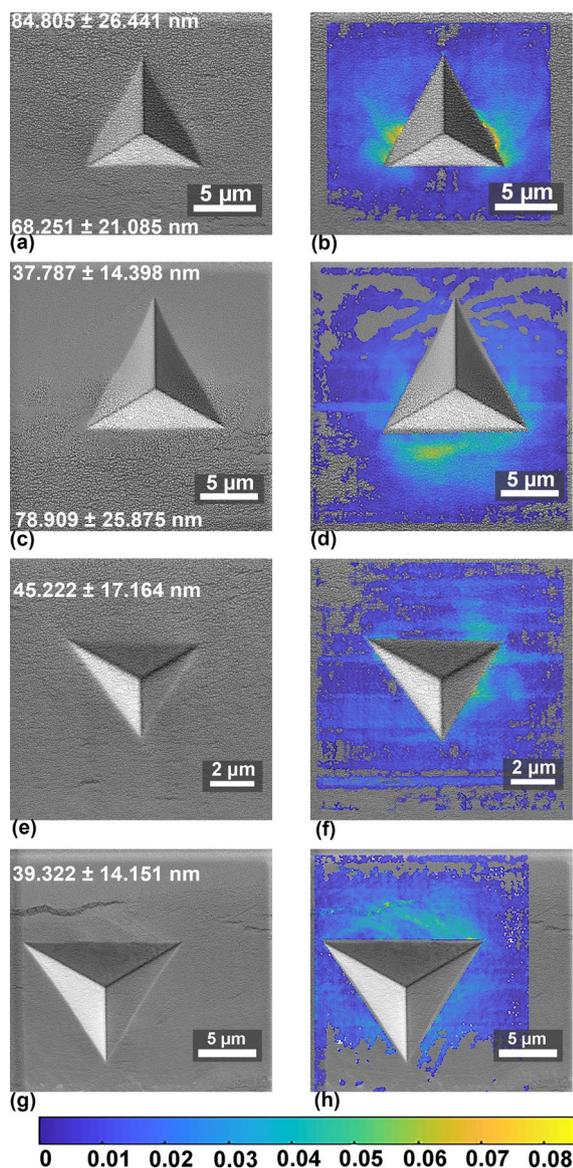
84.805 ± 26.441 nm

68.251 ± 21.085 nm

(a) (b)

37.787 ± 14.398 nm

78.909 ± 25.875 nm

(c) (d)

45.222 ± 17.164 nm

(e) (f)

39.322 ± 14.151 nm

(g) (h)

0 0.01 0.02 0.03 0.04 0.05 0.06 0.07 0.08

Figure 6: Post-indentation SEM images with ligament size marked in white text for (a) F, (c) G, (e) H, and (g) I. Norm of the deviatoric strain for (b) F, (d) G, (f) H, and (h) I. All deviatoric strain plots are associated with a single color bar, shown at the bottom. Locations with no color correspond to strains that fall below the detection limit.

by Fig. 8d, which shows lines of high deviatoric strain spanning from the top indent edge to the Cu-rich vein. These slip bands are also discernible in the SEM image (Fig. 8a, b), though they do not stand out as clearly as in the deviatoric strain map. These flow patterns may be due to the relatively lower hardness in the single-phase vein as compared to the two-phase composite matrix surrounding it. Previous investigations also found that slip bands may form during indentation in materials with both low strain hardening rates and low hardness/modulus ratios [35].
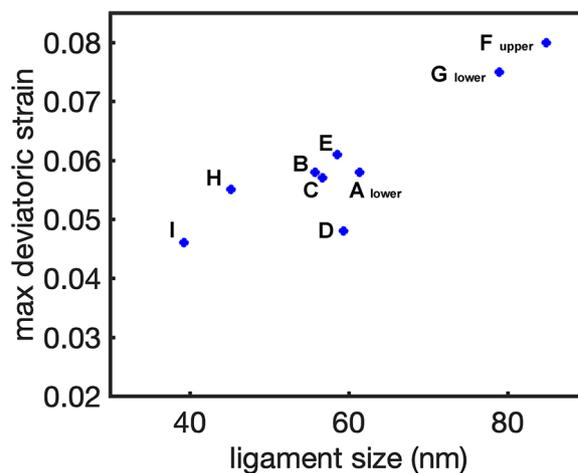

Figure 7: Scatter plot of maximum deviatoric strain and ligament size in indents on SMD CuWTi composite samples.

Assessment of stain partitioning between composite phases

Our DIC analysis determines average strain in an area with dimensions 2–4 times larger than the microstructure dimensions. It does not determine the strain in the constituent phases and therefore cannot tell us whether the phases are co-deforming or whether the strain is concentrating preferentially in one of the two phases. Nevertheless, qualitative assessments of strain partitioning may be performed by comparing pre-indentation images that have been artificially "deformed" by applying the uniform strain computed by DIC with post-indentation images. If the phases co-deform perfectly, then these two images are expected to appear very similar. By contrast, if differences between them are observed, then perfect co-deformation may be ruled out.

To demonstrate this approach, we chose two regions in the area with the largest deviatoric strain in indent G, shown in Fig. 9a. Region 1 has dimensions 226 nm by 226 nm while region 2 has dimensions 107 nm by 166 nm. First, we match contrast and brightness of the pre- and post- indentation images. Next, we take the average strain value of the selected area calculated from DIC ($\varepsilon_{xx}, \varepsilon_{yy}, \varepsilon_{xy}$), and use those values to artificially "strain" the pre-indentation image by performing a linear affine transformation of it. Finally, for ease of comparison, we binarize the pre-indentation, transformed, and post-indentation images into black and white regions. By comparing the image predicted by DIC with the actual strained image, we assess the likelihood of co-deformation.

The results, shown in Fig. 9b, indicate that, in this WCuTi sample, the W-rich and Cu-rich phase do not undergo perfect co-deformation. From DIC, the average deviatoric strain of regions 1 and 2 is ~0.07. Comparing the transformed images with post-indentation images, for both region A and region B, the W-rich (white) phase is significantly different in the actual
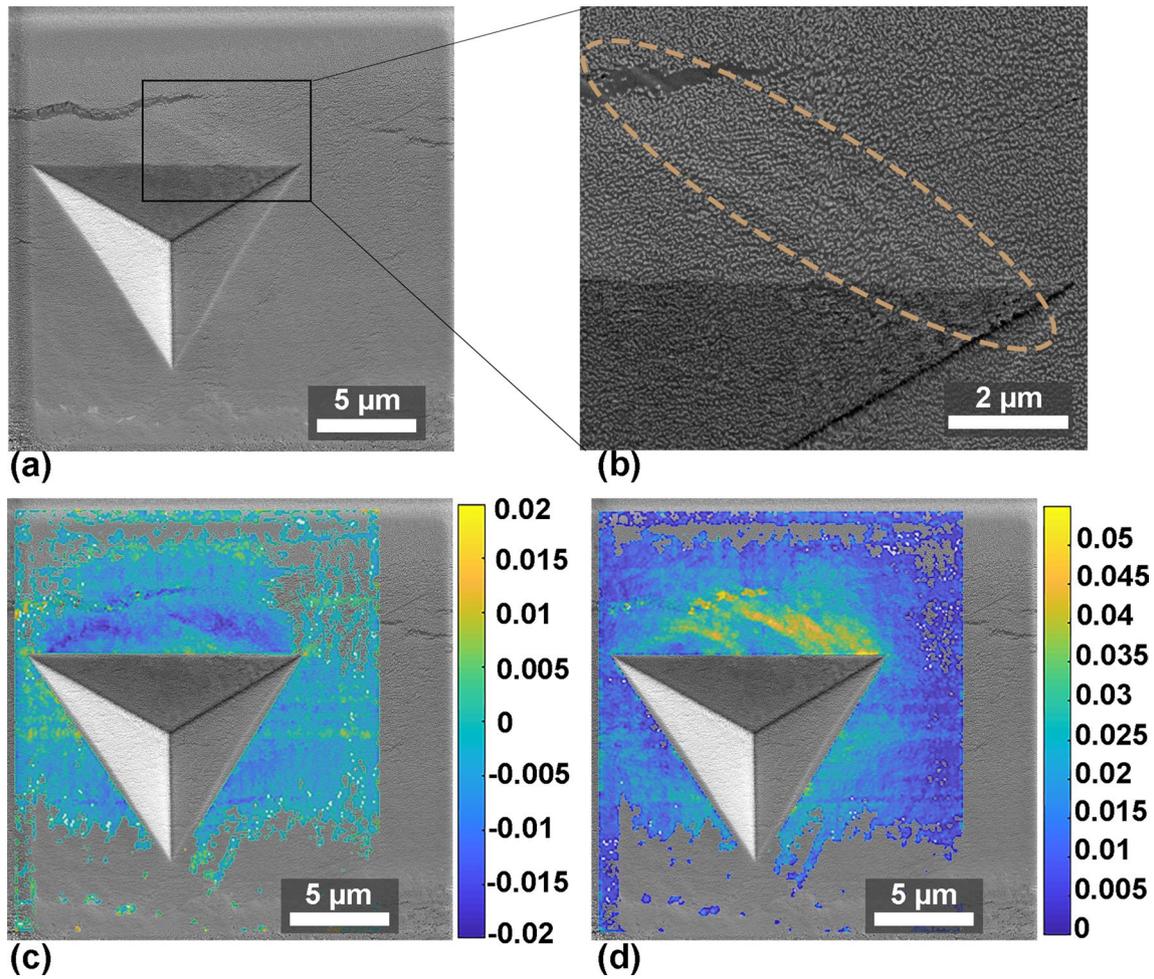
Figure 8: Region I: (a) SEM image; (b) magnified view of the boxed region in (a) with the region containing slip bands marked with an ellipse; (c) hydrostatic strain field; (d) deviatoric strain field.
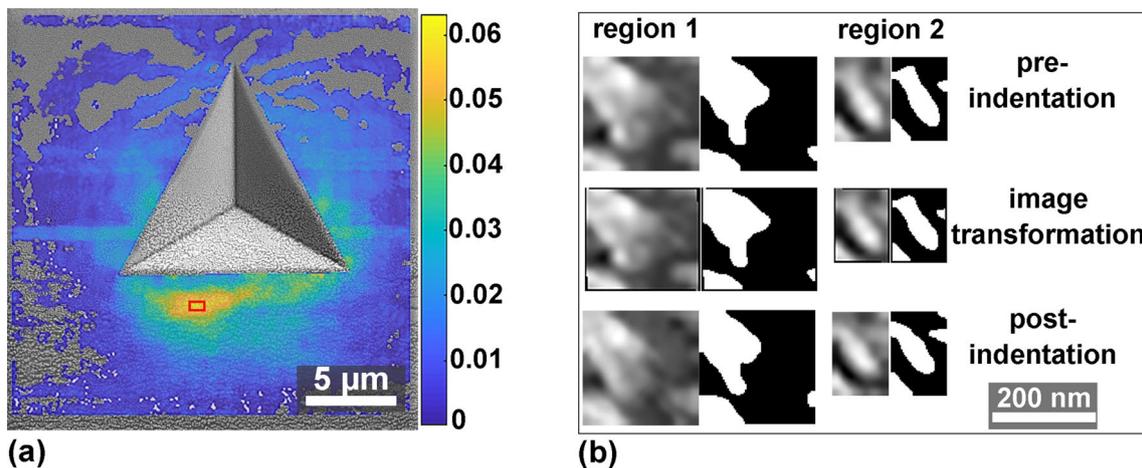

Figure 9: (a) Norm of deviatoric strain around indent G (see Table 1). We assessed co-deformation at two different locations within the red rectangular zone. (b) SEM and binarized pre-indentation, transformed, and post-indentation images for both investigated locations. The W-rich phase appears white in these images.

post-indentation image compared to the transformed image. This observation illustrates that there are local differences in deformation of the two phases. This analysis, however, does not allow us to determine quantitative information, such as which of the two phases deformed more.

Discussion

We have presented a DIC method for characterizing surface strains around small-scale indents. We demonstrated it on indents in a WCuTi nanocomposite. When applying our method, care must be taken to ensure that the SEM images are well suited to analysis via DIC. Specifically, their spatial resolution must be chosen so that distortions in the surface pattern may be resolved. Moreover, surface pattern feature sizes and DIC parameters must be adjusted to reach the best spatial resolution without introducing excessive noise. Finally, the indentation tip angle and depth must be adjusted to avoid edge effects during imaging.

Surface strain determination by DIC provides additional information on indentation response, complementary to load–displacement curves. The latter may be used to characterize hardness and indentation modulus [1, 2], strain rate sensitivity [36], activation volume [37], substrate effects [38], and strain hardening rate [39]. Measurement of surface strains makes it possible to additionally investigate the microstructure-dependence of indentation-induced plasticity. For example, in the present study, we found that the maximum surface strains under indentation are directly correlated to the characteristic microstructure lengths of our samples (Fig. 7). Consistent with this correlation, for indents in regions where there is a gradient in microstructure length scale (e.g., Fig. 6a, c), the surface strains are biased towards regions with larger microstructure lengths. Moreover, in regions of non-uniform microstructure, indentation-induced strains preferentially localize in larger microstructure features (see Fig. 8). Surface strains also allowed us to make estimates of unequal strain partitioning between constituent phases of the material and imperfections in indenter tip alignment.

Beyond the examples given above, future investigations may use surface strains to assess plastic anisotropy effects on indentation response. In an isotropic material, the distribution of surface strains around a conical indenter is expected to be invariant with respect to the position along the circumference of the indent edge. Deviations from such perfect spherical symmetry would therefore be a sign of plastic anisotropy. They may be observed in surface strain distributions. Surface strains may also be used to study interface indentation response: when indenting an interface (grain or phase boundary), surface strains may be used to determine whether the indent is accommodated

equally on both sides of the interface, preferentially on one side, or through deformation along the interface itself. Finally, surface strains may be used to study interactions of indents with surface flaws (e.g., pores, cracks, inclusions, or other indents). By comparing the surface strain of indents as a function of distance from a surface flaw, the distance at which interaction between the indent and the flaw starts to alter the strain field may be determined.

We conducted our work in the SEM. However, DIC analysis of indents may also be carried out in an optical microscope. Our findings have direct bearing on the optimal selection of DIC subset size, pattern size, and indent size for the available spatial resolution for such an experiment. Following the "Resolution adjustment and noise reduction" section and assuming a maximum spatial resolution of 200 nm, characteristic of optical microscopy, we determine an optimal subset size of 5 μm, optimal pattern length scale of 1 μm, and optimal indent size of 50 μm or greater. Artificial patterns for correlation may be deposited on the surface [41] or intrinsic material microstructure may be used as a pattern, provided its characteristic dimensions are on the order of 1 μm, as stated above. In optical microscopy, the phases would have to be distinguished based on differences in surface reflectivity obtained by specific surface preparation methods, found using techniques such as directional reflectivity measurement (DRM) [40].

When collecting SEM images, there are many sources of noise, e.g. signal noise, drift artifacts, and spatial distortion [42]. Previous studies investigated these contributions individually [31, 43] and determined how to reduce them by altering SEM parameters or correct them through numerical analysis. In our work, instead of quantifying each source of noise separately, we accounted for all sources simultaneously to define a detection limit below which strain calculations were not considered reliable. We consider this estimate to be a conservative one. In particular, since some sources of noise are systematic, it may be possible to minimize them via improvements in hardware and software. Doing so would provide the opportunity to reduce the detection limit in our DIC analysis. For example, one possible way to reduce rastering and image drift is by integrating multiple images into a single frame. In this approach, each individual image is taken with low scan time to minimize drift and patterning instabilities [17, 44]. In addition, as those drift artifacts appears in the ε_{yy} strain component of the DIC results, we can rotate the sample by 90°, then use the ε_{xx} DIC results of the rotated pre- and post- indentation images to substitute the original ε_{yy} results. Lenthe et al. [45] applied an external controller to increase acquisition speed while maintaining high image resolution. This controller can be used in future research to reduce rastering drift from the SEM beam.

Due to edge effects in SEM imaging, our DIC-indentation analysis is currently limited to Berkovich indenter tips with

indent depth deeper than ~ 0.45 um. Cube corner, 45°, and 55° indenters did not provide useful in-plane strain information in our study. However, it may be possible to apply the DIC method to such indents if the indent depth is markedly increased. Doing so would provide larger plastically deformed regions around the indent, so the edge effect might only block part of these regions. Moreover, more advanced SEM detectors are able to collect in-beam secondary electrons with a closer working distance, collecting electrons at more nearly perpendicular incidence to the sample surface, thus reducing brightness bias. We applied this method and reduced the brightness bias from the edge effect (Fig. S2b), However, the signal was not strong enough for DIC analysis. Future effort can be applied to find the optimal parameters for in-beam SEM imaging. Moreover, image integration approaches, such as those described in Ref. [44], may help to enhance image signal sufficiently to carry out DIC analysis. Backscattered electron detectors might also help to reduce the edge effect, provided the collected signal is sufficiently strong.

Since the surface strain distribution is very sensitive to tip alignment, indenter tips must be well calibrated to yield mutually comparable surface strain maps across multiple indentation tests. Indeed, DIC may provide a method for checking the alignment, e.g. by characterizing surface strains on a well-studied reference sample, such as a single crystal with a specific surface facet orientation. Unlike the dealloyed samples investigated here, single crystals do not have any inherent pattern that may be used for DIC. However, there are many ways to apply speckle patterns suitable for DIC onto single crystals [25]. By performing multiple indents followed by DIC, the tip alignment may be adjusted until the strain distribution matches the reference distribution.

The SMD WCuTi composite does not perfectly co-deform in our indentation test. The location where we assess the strain partitioning, indent G, has a ligament size of around 78 nm. Lack of co-deformation at the nanometer-level scale of the ligament dimensions it actually to be expected, as plastic flow at these dimensions likely proceeds within discrete slip bands. While DIC has been used repeatedly to resolve slip bands within grains [46, 47], such analyses have not been carried out with grains or features smaller than 100 nm. The ability to resolve nanometer-scale slip events will require significant advances in imaging and analysis.

The out-of-plane displacement might influence the DIC analysis. In this research, we exclude regions of significant out-of-plane displacement from our DIC analysis, limiting it instead to areas where the displacement can reasonably be approximated as being in-plane only. We also estimate the error in the inferred surface strains arising from the neglect of out-of-plane displacements in the region analyzed by DIC, and the error is deemed acceptable for our study. Future developments may also assess the potential to characterize the full, 3-d tensor of surface plastic strains by integrating the in-plane and out-of-plane deformation fields. New methods for combing SEM with confocal microscopy, adapting stereoscopic techniques available in optical DIC [48], would be of great value for gathering full 3-d plastic strain profiles.

Our findings provide new opportunities for comparisons between indentation experiments and computer simulations. Strain distributions underneath indents and their relation to surface deformation have been extensively modeled by finite element analysis method (FEM) [49] and molecular dynamics [50]. For example, Alcala et al. used finite element analysis to model spherical and Berkovich indentation into a single crystal fcc material. They investigated the spatial distribution of active slip systems and related it to surface strain features, such as rosette formation [49]. The integration of experimental analysis with FEM simulation would provide further quantitative insight on both in-plane and out-of-plane deformation, with the consideration of phase morphology in composite materials or the effect of interfaces and impurities. Surface strain profiling may also be combined to characterize the stress–strain response of the material more fully [51].

Future research can make use of surface strains around indents to improve inferences of material properties. For example, Zhang et al. [52] used Bayesian statistics and FEM simulations of indentation to show that surface profiles may be used to infer strain hardening exponents from indentation tests. Such inferences may also be possible based on surface strain distributions. Future experimental efforts may exploit the higher symmetry of conical indenters to facilitate comparisons with such models.

Conclusion

The work we presented here demonstrates a method for assessing local plastic strains around micro-scale indents by SEM-DIC. This method may be applied to materials with intrinsic or extrinsic surface patterns. It provides additional information beyond load–displacement curves from indentation tests, such as 2-D in-plane strain distributions, heterogeneous mechanical response, and strain partitioning between phases.

We applied this approach to study the indentation response of dealloyed WTi/CuTi nanocomposites, obtaining the in-plane strain field around an indent with sub-micron resolution. We analyzed the indentation-induced surface strain distribution as a function of indentation depth and indenter angle. For samples with comparable microstructure feature dimensions, the maximum magnitude of surface strain does not change with the indentation depth. In addition, strain concentrates preferentially in areas with larger microstructure feature dimensions. Finally, we find that the constituent phases in WCuTi composites do not perfectly co-deform.

Methodology

Liquid metal dealloying (LMD) follows the procedure detailed in Ref. [53]. 20 g of $Ti_{65}W_{35}$ master alloy was prepared by radio-frequency induction melting under a flowing Ar atmosphere (99.999 wt.%) and annealed under flowing Ar (99.999 wt.%) for approximately 20 h to ensure compositional homogeneity. For LMD, we cut a 0.5 cm^3 ingot from the master alloy using wire electrical discharge machining and fabricated the WTi/CuTi composite by selectively dissolving Ti from $Ti_{65}W_{35}$ in molten Cu at 1200 °C for 10 min.

Solid metal dealloying (SMD) composites were synthesized as in Ref. [27]. Initial alloy preparation followed the process in Ref. [53]. A 20 g $Ti_{80}W_{20}$ master alloy was prepared by radio-frequency induction heating under flowing Ar (99.999 wt.%), and homogenized under flowing Ar (99.999 wt.%) for approximately 40 h. A 1.5 cm^2, 1 mm-thick $Ti_{80}W_{20}$ disk was cut from the master alloy using wire electrical discharge machining and bonded between two 1 mm Cu sheets at 820 °C for 10 min using a 30 μm-thick $Cu_{38}Ag_{62}$ braze. The W/Cu bicontinuous composite was fabricated via solid phase dealloying by heating the $Ti_{80}W_{20}$/Cu diffusion couple in a sealed quartz tube under ultra-high purity Ar (99.999 wt.%) at three different temperatures (600, 700, 750 °C) and for two different durations (48 and 200 h). This procedure resulted in dealloying depths ranging from ~ 30 to ~ 55 μm and constituent phase dimensions ranging from ~ 40 to ~ 100 nm. The surfaces of both LMD and SMD samples were prepared for characterization and testing using a grinding step of 600 grit, polishing steps using 9, 3, and 1 μm diamond particles, and a final polishing step using 0.05 μm colloidal silica.

SEM images were taken using a Tescan FERA3 FIB-SEM. All SEM images were acquired under a long dwell time of 100 μs/pixel, with high voltage of 10 kV, and beam current ranging from 275 to 345 mA. We acquire images at 16-bits per pixel with size no smaller than 1280 × 1280 pixels. The pixel dimensions and field of view for each SEM image depend on the magnification, which we adjust depending on each specimen's microstructure feature dimensions (as detailed in the "Resolution adjustment and noise reduction" section).

Indentation testing was performed using a Hysitron TI 950 Triboindenter with a standard Berkovich tip to generate fiducial markers as well as indents with different depths. All indents were quasistatic with a 5–2–5 s trapezoidal load function. Surface profiles were obtained by AFM using a Bruker Dimension Icon instrument with a scan speed of 0.3 Hz and a scan area of 70 × 70 $μm^2$.

Surface profiles of SMD samples with indents were measured by a laser confocal microscope (Keyence 3D laser scanning confocal microscope VK-X1000). The resolutions of the measurement were 50 nm in plane (x and y directions) and 20 nm out of plane (z direction). For the selected region, the laser scan focused on the highest to the lowest elevation level of that region for the upper and lower limit. We corrected the image tilt by selecting multiple surface points out of the indent area, and set the sample surface as the baseline with height of zero.

Supplementary information

The online version contains supplementary material available at https://doi.org/10.1557/s43578-020-00019-y.

References

1. W.C. Oliver, G.M. Pharr, An improved technique for determining hardness and elastic modulus using load and displacement sensing indentation experiments. J. Mater. Res. **7**(6), 1564 (1992)

2. W.C. Oliver, G.M. Pharr, Measurement of hardness and elastic modulus by instrumented indentation: advances in understanding and refinements to methodology. J. Mater. Res. **19**(1), 3 (2004)

3. N.A. Sakharova, J.V. Fernandes, J.M. Antunes, M.C. Oliveira, Comparison between Berkovich, Vickers and conical indentation tests: a three-dimensional numerical simulation study. IJSS **46**(5), 1095 (2009)

4. Z. Wang, T.G. Murthy, C. Saldana, Deformation field interaction in sequential circular indentation of a strain hardening material. Philos. Mag. **99**(10), 1259 (2019)

5. R.I. Barabash, H. Bei, Y.F. Gao, G.E. Ice, Indentation-induced localized deformation and elastic strain partitioning in composites at submicron length scale. Acta Mater. **58**(20), 6784 (2010)

6. D. Zhao, H. Zhao, B. Zhu, S. Wang, Investigation on hardening behavior of metallic glass under cyclic indentation loading via molecular dynamics simulation. Appl. Surf. Sci. **416**, 14 (2017)

7. G. Srikant, N. Chollacoop, U. Ramamurty, Plastic strain distribution underneath a Vickers Indenter: role of yield strength and work hardening exponent. Acta Mater. **54**(19), 5171 (2006)

8. C. Bermudo, L. Sevilla, G.C. Lopez, Material flow analysis in indentation by two-dimensional digital image correlation and finite elements method. Materials. **10**(6), 674 (2017)

9. I. McCue, S. Xiang, K. Xie, M.J. Demkowicz, The effect of microstructure morphology on indentation response of Ta/Ti nanocomposite thin films. MMTA **51**, 5677–5690 (2020)

10. N.Q. Chinh, P. Szommer, Z. Horita, T.G. Langdon, Experimental evidence for grain-boundary sliding in ultrafine-grained aluminum processed by severe plastic deformation. Adv Mater. **18**(1), 34 (2006)

11. C. Tromas, P. Villechaise, V. Gauthier-Brunet, S. Dubois, Slip line analysis around nanoindentation imprints in Ti3SnC2: a new insight into plasticity of MAX-phase materials. Philos. Mag. **91**(7–9), 1265 (2011)

12. T. Scholz, K.K. McLaughlin, F. Giuliani, W.J. Clegg, F.J. Espinoza-Beltrán, M.V. Swain, G.A. Schneider, Nanoindentation initiated dislocations in barium titanate (BaTiO3). Appl. Phys. Lett. **91**(6), 062903 (2007)

13. A.J. Gayle, L.H. Friedman, R. Beams, B.G. Bush, Y.B. Gerbig, C.A. Michaels, M.D. Vaudin, R.F. Cook, Two-dimensional strain-mapping by electron backscatter diffraction and confocal Raman spectroscopy. J. Appl. Phys. **122**(20), 205101 (2017)

14. A.J. Wilkinson, T.B. Britton, J. Jiang, P.S. Karamched, A review of advances and challenges in EBSD strain mapping. IOP Conf Ser. **55**, 012020 (2014)

15. A.J. Wilkinson, G. Meaden, D.J. Dingley, High resolution mapping of strains and rotations using electron backscatter diffraction. Mater. Sci. Technol. **22**(11), 1271 (2006)

16. K. Genovese, A. Montes, A. Martínez, S.L. Evans, Full-surface deformation measurement of anisotropic tissues under indentation. Med. Eng. Phys. **37**(5), 484 (2015)

17. M.A. Sutton, N. Li, D. Joy, A.P. Reynolds, X. Li, Scanning electron microscopy for quantitative small and large deformation measurements part I: SEM imaging at magnifications from 200 to 10,000. ExM. **47**(6), 775 (2007)

18. M.A. Sutton, N. Li, D. Garcia, N. Cornille, J.J. Orteu, S.R. McNeill, H.W. Schreier, X. Li, A.P. Reynolds, Scanning electron microscopy for quantitative small and large deformation measurements Part II: experimental validation for magnifications from 200 to 10,000. ExM. **47**(6), 789 (2007)

19. J.C. Stinville, M.P. Echlin, D. Texier, F. Bridier, P. Bocher, T.M. Pollock, Sub-grain scale digital image correlation by electron microscopy for polycrystalline materials during elastic and plastic deformation. ExM. **56**(2), 197 (2016)

20. J.C. Stinville, N. Vanderesse, F. Bridier, P. Bocher, T.M. Pollock, High resolution mapping of strain localization near twin boundaries in a nickel-based superalloy. Acta Mater. **98**, 29 (2015)

21. J.S. Merson, M.B. Prime, M.L. Lovato and C. Liu: In-situ DIC and strain gauges to isolate the deficiencies in a model for indentation including anisotropic plasticity, in residual stress, thermo-mechanics & infrared imaging, hybrid techniques and inverse problems, vol. 9: Proceedings of the 2015 Annual Conference on Experimental and Applied Mechanics. edited by S. Bossuyt, G. Schajer and A. Carpinteri (Springer International Publishing, Berlin, 2016), pp. 183.

22. J.C. Kuo, S.H. Tung, M.H. Shih, Y.Y. Lu, Characterisation of indentation-induced pattern using full-field strain measurement. Strai. **46**(3), 277 (2010)

23. J. Valach, D. Kytýř, N. Fenclová, P. Koudelka, T. Doktor, T. Fíla: evaluation of local plastic flow in the vicinity of indentation by the means of DIC applied on SEM micrographs. In Key Eng. Mater., edited by L. Pešek and P. Zubko (**586**, Trans Tech Publ, City, 2014), pp. 257.

24. I.D. McCue: Frontiers of dealloying-novel processing for advanced materials, in MSEng, (Johns Hopkins University, Baltimore, 2015).

25. Y.L. Dong, B. Pan, A review of speckle pattern fabrication and assessment for digital image correlation. Exp. Mech. **57**, 1161–1181 (2017)

26. P.A. Geslin, I. McCue, B. Gaskey, J. Erlebacher, A. Karma, Topology-generating interfacial pattern formation during liquid metal dealloying. Nat Commun. **6**, 8887 (2015)

27. J. Stuckner, K. Frei, I. McCue, M.J. Demkowicz, M. Murayama, AQUAMI: an open source python package and GUI for the automatic quantitative analysis of morphologically complex multiphase materials. Comput. Mater. Sci. **139**, 320 (2017)

28. J. Blaber, B. Adair, A. Antoniou, Ncorr: open-source 2D digital image correlation matlab software. ExM. **55**(6), 1105 (2015)

29. P.L. Reu, E. Toussaint, E. Jones, H.A. Bruck, M. Iadicola, R. Balcaen, D.Z. Turner, T. Siebert, P. Lava, M. Simonsen, DIC challenge: developing images and guidelines for evaluating accuracy and resolution of 2D analyses. ExM. **58**(7), 1067 (2018)

30. P. Zhou, K.E. Goodson, Subpixel displacement and deformation gradient measurement using digital image/speckle correlation (DISC). OptEn. **40**(8), 1613 (2001)

31. A.D. Kammers, S. Daly, Digital image correlation under scanning electron microscopy: methodology and validation. ExM. **53**(9), 1743 (2013)

32. B. Pan, A. Asundi, H. Xie, J. Gao, Digital image correlation using iterative least squares and pointwise least squares for displacement field and strain field measurements. OptLE. **47**(7), 865 (2009)

33. H. Seiler, Secondary electron emission in the scanning electron microscope. J. Appl. Phys. **54**(11), R1 (1983)

34. W.D. Nix, H. Gao, Indentation size effects in crystalline materials: a law for strain gradient plasticity. J. Mech. Phys. Solids. **46**(3), 411 (1998)

35. A. Bolshakov, G.M. Pharr, Influences of pileup on the measurement of mechanical properties by load and depth sensing indentation techniques. J. Mater. Res. **13**(4), 1049 (1998)

36. J. Lu, S. Suresh, G. Ravichandran, Dynamic indentation for determining the strain rate sensitivity of metals. J. Mech. Phys. Solids. **51**(11), 1923 (2003)

37. V. Maier-Kiener, K. Durst, Advanced nanoindentation testing for studying strain-rate sensitivity and activation volume . JOM. **69**(11), 2246 (2017)

38. Z.S. Ma, Y.C. Zhou, S.G. Long, C. Lu, On the intrinsic hardness of a metallic film/substrate system: Indentation size and substrate effects. Int. J. Plast. **34**, 1 (2012)

39. A.K. Bhattacharya, W.D. Nix, Finite element simulation of indentation experiments. IJSS. **24**(9), 881 (1988)

40. M. Seita, M.M. Nimerfroh, M.J. Demkowicz, Acquisition of partial grain orientation information using optical microscopy. Acta Mater. **123**, 70 (2017)

41. Y.L. Dong, B. Pan, A review of speckle pattern fabrication and assessment for digital image correlation. ExM. **57**(8), 1161 (2017)

42. M.A. Sutton, J.J. Orteu, H. Schreier, *Image Correlation for Shape, Motion and Deformation Measurements: Basic Concepts, Theory and Applications* (Springer Science & Business Media, Berlin, 2009).

43. M.A. Sutton, N. Li, D. Garcia, N. Cornille, J.J. Orteu, S.R. McNeill, H.W. Schreier, X. Li, Metrology in a scanning electron microscope: theoretical developments and experimental validation. Meas. Sci. Technol. **17**(10), 2613 (2006)

44. C. Mansilla, V. Ocelík, J.T.M. De Hosson, A new methodology to analyze instabilities in SEM imaging. Microsc Microanal. **20**(6), 1625 (2014)

45. W.C. Lenthe, J.C. Stinville, M.P. Echlin, Z. Chen, S. Daly, T.M. Pollock, Advanced detector signal acquisition and electron beam scanning for high resolution SEM imaging. Ultmi. **195**, 93 (2018)

46. M. Henning, H. Vehoff, Local mechanical behavior and slip band formation within grains of thin sheets. Acta Mater. **53**(5), 1285 (2005)

47. R. Jiang, F. Pierron, S. Octaviani, P.A.S. Reed, Characterisation of strain localisation processes during fatigue crack initiation and early crack propagation by SEM-DIC in an advanced disc alloy. Mater. Sci. Eng. A. **699**, 128 (2017)

48. J. Tong, B. Lin, Y.-W. Lu, K. Madi, Y. Tai, J. Yates, V. Doquet, Near-tip strain evolution under cyclic loading: in situ experimental observation and numerical modelling. Int. J. K. Fatigue. **71**, 45 (2015)

49. J. Alcalá, D. Esqué-de los Ojos, J. Očenášek, Continuum crystal plasticity analyses of the plastic flow features underneath single-crystal indentations. Philos. Mag. **91**(7–9), 1050 (2011)

50. A.-S. Tran, Z.-H. Hong, M.-Y. Chen, T.-H. Fang, Incipient plasticity and indentation response of MgO surfaces using molecular dynamics. Mater. Res. Express. **5**(5), 055017 (2018)

51. S. Pathak, S.R. Kalidindi, Spherical nanoindentation stress–strain curves. Mater. Sci. Eng. **91**(1), 36 (2015)

52. Y. Zhang, J.D. Hart, A. Needleman, Identification of plastic properties from conical indentation using a bayesian-type statistical approach. J. Appl. Mech. **86**(1), 011002 (2018)

53. I. McCue, B. Gaskey, P.-A. Geslin, A. Karma, J. Erlebacher, Kinetics and morphological evolution of liquid metal dealloying. Acta Mater. **115**, 10 (2016)